ROYAL SOCIETY
OF CHEMISTRY

COMMUNICATION

Check for updates

Ionic liquid pre-intercalated MXene films for ionogel-based flexible micro-supercapacitors with high volumetric energy density†

Shuanghao Zheng,‡[abc] Chuanfang (John) Zhang,‡[d] Feng Zhou,[a] Yanfeng Dong,[a] Xiaoyu Shi,[abe] Valeria Nicolosi,[d] Zhong-Shuai Wu [ID] *[a] and Xinhe Bao [ID] [ab]

MXenes are emerging as a very promising electrode material of high-performance micro-supercapacitors (MSCs) for microscale electronics. However, MXene based MSCs (M-MSCs) reported so far exhibit low areal ($\leq$10 μW h cm^{-2}) and volumetric ($\leq$20 mW h cm^{-3}) energy densities due to their narrow working voltage in aqueous systems (0.6–1.0 V). Herein, we report for the first time the construction of high-voltage and high-energy flexible ionogel-based M-MSCs with interdigital microelectrodes of ionic liquid pre-intercalated MXene films. Benefitting from the pre-intercalation of ionic liquid, the as-fabricated M-MSCs, working at 3 V in 1-ethyl-3-methylimidazolium tetrafluoroborate (EMIMBF$_4$), exhibited high areal and volumetric energy densities of 13.9 μW h cm^{-2} and 43.7 mW h cm^{-3}, respectively, both of which are among the highest values for the reported M-MSCs. Moreover, all-solid-state M-MSCs using ionogel electrolytes displayed exceptional flexibility without capacitance loss under various deformation conditions and seamless integration free of metal-based interconnections for boosting voltage output. Therefore, such high-energy M-MSCs hold great potential for direct integration of flexible and miniature electronics.

The dramatic development of wearable and miniature electronics, *e.g.*, microelectromechanical systems, microrobots, and microsensors, has greatly accelerated the exploitation of high-performance microscale electrochemical energy storage units that are small and flexible enough to be strongly coupled with

such electronics.[1–6] Recently, micro-supercapacitors (MSCs), with in-plane microelectrode geometry on a single substrate, have been gradually acknowledged as a novel class of highly competitive miniaturized energy storage devices,[7–9] possessing remarkable merits of ultrafast charge–discharge rate, ultrahigh power density, long-term cyclability, outstanding safety, and being separator-free.[10–13] To date, great efforts have been concentrated on the performance tailoring of planar MSCs based on different electrode materials, for instance, nano-carbons (*e.g.*, carbide derived carbon,[14] onion-like carbon,[15] carbon nanotubes,[16] and graphene[17–20]), MXenes,[21–24] conducting polymers,[25,26] and metal oxides[27] and hydroxides.[28] Among them, atomically thin two-dimensional (2D) materials with an intrinsically flat and flexible structure can match well with the in-plane geometry of MSCs, in which the electrolyte ions are capable of fully utilizing the flat architecture and ultrathin thickness of 2D materials and realizing fast ionic diffusion along the plane direction of 2D nanosheet-based nano-channels.[29] Consequently, graphene and other analogous 2D nanosheets are regarded as promising electrode materials for the creation of planar MSCs.[30] However, both the areal and volumetric energy densities of most reported 2D nanosheet-based MSCs still fail to compete with those of commercially available lithium thin-film microbatteries ($\leq$10 mW h cm^{-3}) for miniaturized electronics and self-powered microsystems.[15]

MXenes are an emerging large family of 2D early transition metal carbides and carbonitrides from the 60+ group of MAX phases, with engineered surface chemistry and exceptional ion intercalation behavior, having tremendous potential for numerous energy storage devices from batteries to super-capacitors.[31–39] In particular, Ti$_3$C$_2$T$_X$ is the most widely studied MXene for supercapacitors with an ultrahigh volumetric capacitance up to 1500 F cm^{-3} and ultrahigh electrical conductivity ($\sim$9800 S cm^{-1}), outperforming most reported electrode materials.[40–42] Unfortunately, high volumetric capacitance of such Ti$_3$C$_2$T$_X$ MXene based MSCs (M-MSCs) is normally obtained in aqueous electrolytes, with a very limited cell voltage of 0.6–1.0 V in a symmetric configuration. Therefore, the

[a]Dalian National Laboratory for Clean Energy, Dalian Institute of Chemical Physics, Chinese Academy of Sciences, 457 Zhongshan Road, Dalian 116023, China. E-mail: wuzs@dicp.ac.cn

[b]State Key Laboratory of Catalysis, Dalian Institute of Chemical Physics, Chinese Academy of Sciences, 457 Zhongshan Road, Dalian 116023, China

[c]University of Chinese Academy of Sciences, 19 A Yuquan Rd, Shijingshan District, Beijing, 100049, China

[d]CRANN, AMBER, School of Chemistry, Trinity College Dublin, Dublin 2, Ireland

[e]Department of Chemical Physics, University of Science and Technology of China, 96 JinZhai Road, Hefei 230026, China

† Electronic supplementary information (ESI) available. See DOI: 10.1039/c9ta02190f

‡ These authors contributed equally to this work.

9478 | *J. Mater. Chem. A*, 2019, **7**, 9478–9485

This journal is © The Royal Society of Chemistry 2019

resulting MSCs exhibited low areal ($\leq$10 μW h cm^{-2}) and volumetric ($\leq$20 mW h cm^{-3}) energy density.[22,24,43,44] On the other hand, using an ionic liquid as the electrolyte can significantly broaden the voltage window of supercapacitors, but two reported MXene based cells operated at 3 V so far still offer low gravimetric capacitance (80 F g^{-1}) and unsatisfactory cycling stability.[45,46] To realize high-density electrochemical capacitive energy storage, Li's group developed a general strategy to create liquid electrolyte-mediated graphene compact films, with a high ion-accessible surface area and low ion transport resistance, for boosting the volumetric energy density of supercapacitors to 60 W h L^{-1}.[47] Nevertheless, rational design and construction of ionic liquid mediated MXene films for high energy MSCs remains undeveloped.

Here, we reported the on-chip fabrication of a new type of high-voltage ionogel-based MSC with interdigital microelectrode fingers of ionic liquid pre-intercalated MXene films, simultaneously achieving high volumetric energy density, exceptional flexibility and modular integration of bipolar cells. With interdigital mask-assisted deposition of MXene and graphene, the resulting interdigital microelectrodes possessed an outstanding electrical conductivity of 2200 S cm^{-1} without a polymer binder and conductive additives as well as metal current collectors. Benefitting from the pre-intercalation of

ionic liquids, MXene based electrode films continuously developed an ion transport network with an expanded interlayer spacing of 1.45 nm, which is larger than that of the fresh undried MXene (1.27 nm) and fully dried MXene (1.09 nm). The resulting MSCs, assembled with the EMIMBF$_4$ pre-intercalated films and tested in the same electrolyte of EMIMBF$_4$, delivered a remarkably high volumetric capacitance of 140 F cm^{-3}, high areal energy density of 13.9 μW h cm^{-2} and volumetric energy density of 43.7 mW h cm^{-3}, the latter two of which are the highest values of the state-of-the-art M-MSCs reported. Notably, all-solid-state MSCs using an ionogel electrolyte composed of EMIMBF$_4$ and poly(vinylidene fluoride-hexafluoropropylene) (EMIMBF$_4$/PVDF-HFP) also exhibited a high areal energy density of 13.3 μW h cm^{-2} and volumetric energy density of 41.8 mW h cm^{-3}, accompanied by long-term cyclability up to 10 000 cycles. Furthermore, our ionogel based MSCs showed outstanding flexibility without capacitance degradation under repeated deformation conditions, and are readily integrated without any requirement of metal interconnection to increase output voltage and capacitance.

The fabrication of M-MSCs is schematically elucidated in Fig. 1a. Typically, four steps were involved. Firstly, the interdigital patterns of MXene microelectrodes (1.6 mL, 0.65 mg mL^{-1}) were created with the assistance of an interdigital mask.
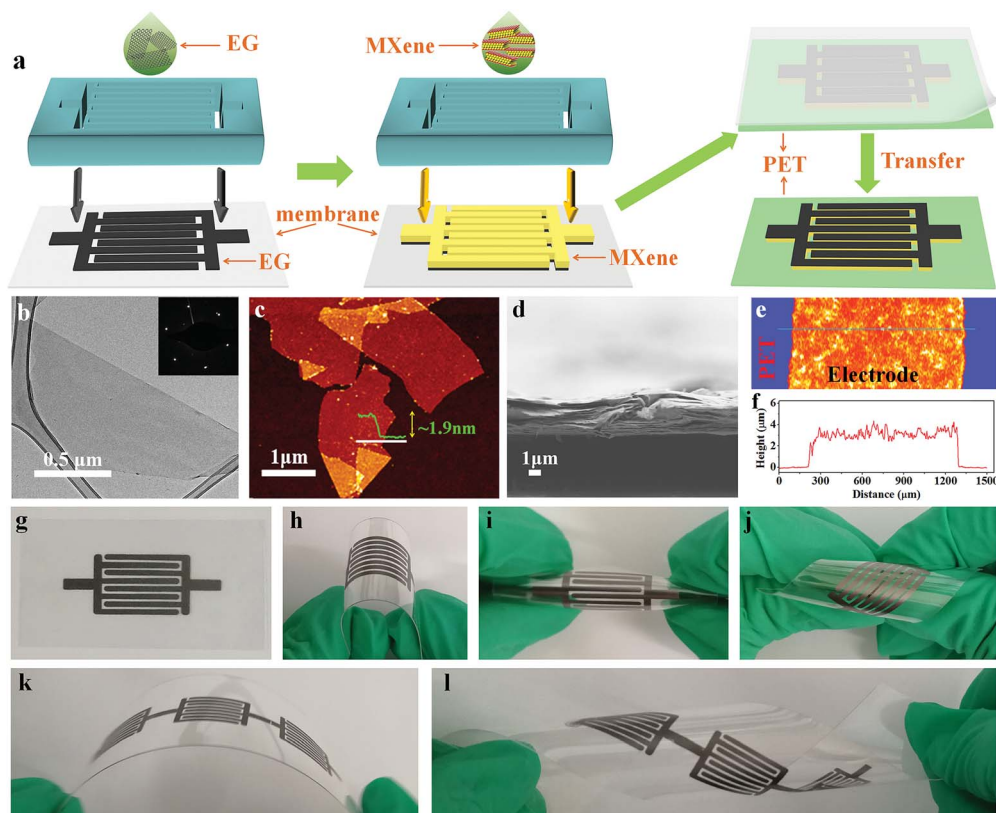

Fig. 1 Fabrication and characterization of M-MSCs. (a) Schematic of the fabrication of M-MSCs. (b) TEM image of MXene. The inset shows a selected area electron diffraction image. (c) Atomic force microscopy image of single-layer MXene nanosheets. The inset shows the height profile. (d) Cross-sectional SEM image and (e) surface profile map of a microelectrode finger. (f) Height profile of a microelectrode finger of M-MSCs. (g–j) Photographs of M-MSCs in flat (g), bending (h and i) and twisting (j) states. (k and l) Photographs of three serially connected M-MSCs in bending (k) and spiral (l) states.

This journal is © The Royal Society of Chemistry 2019

J. Mater. Chem. A, 2019, **7**, 9478–9485 | **9479**

The ultrathin $Ti_3C_2T_X$ MXene nanosheets, with a typical lateral size of 1–3 μm (Fig. 1b) and single-layer thickness of 1.9 nm (Fig. 1c),[48] were prepared by etching the Ti_3AlC_2 MAX phase with a LiF/HCl solution.[24,39,49] It is worth noting that, to construct the highly uniform MXene film and ensure the following full transfer of microelectrodes from the filtration membrane onto the flexible substrate, we selected high-quality, large-size and solution-processable electrochemically exfoliated graphene (EG, 2 mL, 0.1 mg mL^{-1}, Fig. S1†) as the bottom-layer flexible elastic support on a polyvinylidene fluoride (PVDF) membrane, which is critical for uniform deposition of MXene films. Secondly, the resulting patterned MXene-based microelectrodes were directly transferred onto a flexible polyethylene terephthalate (PET) substrate under 20 MPa pressure. Without the bottom EG layer, the interdigital MXene layer readily suffered from short circuit. Benefitting from the metallic conductivity of MXene nanosheets, the microelectrodes exhibited a high electrical conductivity of ∼2200 S cm^{-1} (Fig. S2†), enabling fast electron transport without the need for a metal-based current collector. Cross-sectional scanning electron microscopy (SEM) images (Fig. 1d and S3†) display the uniform layer-stacked structure of microelectrode films, which is highly favorable for the fast transport of ions along the flat plane of MXene nanosheets. The surface profile (Fig. 1e) revealed the large-scale flat uniformity of the microelectrode fingers, with a stacking density of 2.1 g cm^{-3} and an average thickness of ∼3.2 μm (Fig. 1f and S4†). Remarkably, the obtained M-MSCs (Fig. 1g) exhibited excellent flexibility without any fragmentation of electrode films and delamination between microelectrode films and the PET substrate under severe deformation conditions, e.g., serious bending (Fig. 1h and i) and twisting (Fig. 1j) states.

Moreover, integrated M-MSCs connected in series or in parallel, such as three serially connected M-MSCs in bending (Fig. 1k) and spiral (Fig. 1l) states, can be readily realized through a one by one transfer strategy, and displayed extraordinary flexibility without any degradation. Thirdly, the obtained fresh undried microelectrodes were completely immersed into the test ionic liquid electrolytes (e.g., EMIMBF$_4$) for 24 h under vacuum conditions. Finally, the corresponding electrolyte, e.g., EMIMBF$_4$ or EMIMBF$_4$/PVDF-HFP, was drop-cast onto the finger area of interdigital microelectrodes, and high-voltage ionic liquid or ionogel based M-MSCs were achieved.

To highlight the importance of ionic liquid pre-intercalation into the MXene film for the performance improvement of M-MSCs, we fabricated two kinds of M-MSCs, one is denoted as PM-MSCs based on the ionic liquid pre-intercalated MXene (PM) film after sufficient immersion in EMIMBF$_4$ for 24 h, and the other is denoted as DM-MSCs based on the fully dried MXene (DM) film at 120 °C for 24 h under vacuum for comparison. As expected, X-ray diffraction (XRD) patterns (Fig. 2b and S5†) disclosed that the (002) diffraction peak of the PM film downshifts to 6.1°, corresponding to an enlarged interlamellar spacing of 1.45 nm, resulting from the intercalation of ionic liquid, in comparison with that of the freshly undried MXene film having an interlayer spacing of 1.27 nm at 7.0°. In a sharp contrast, the (002) diffraction peak of the DM film upshifts to 8.1°, with a decreased interlayer spacing of 1.09 nm due to the removal of residual water from the freshly undried MXene film. Note that the vacuum-annealing treatment didn't induce the oxidation of MXene films, as demonstrated from Raman spectra (Fig. S6†).
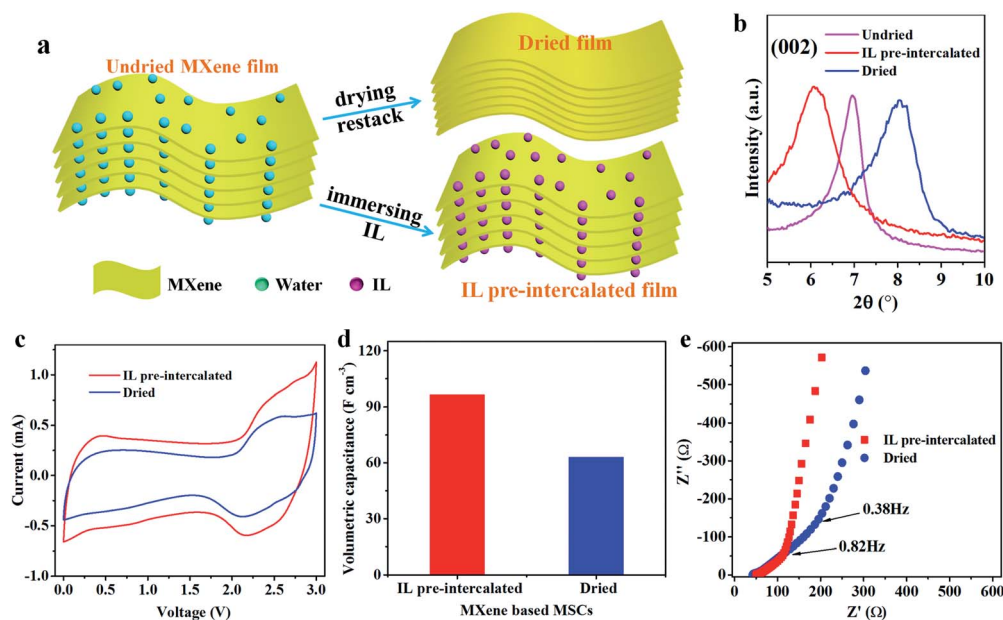

Fig. 2 Comparison of EMIMBF$_4$ pre-intercalated and dried MXene films for M-MSCs, tested in EMIMBF$_4$. (a) Schematic of the preparation of ionic liquid (IL) pre-intercalated and dried MXene electrode films. (b) XRD patterns of IL pre-intercalated and dried MXene films in comparison with that of the freshly undried film. (c) CV curves tested at 50 mV s^{-1}, (d) volumetric capacitance, and (e) EIS spectra of M-MSCs based on an IL pre-intercalated film and a dried MXene film.

9480 | J. Mater. Chem. A, 2019, 7, 9478–9485

This journal is © The Royal Society of Chemistry 2019

To further verify this disparity, the electrochemical performances of PM-MSCs and DM-MSCs were evaluated in EMIMBF$_4$ at a voltage of 3 V, tested at 50 mV s^{-1}. Apparently, the cyclic voltammetry (CV) curve of PM-MSCs exhibited a larger integration area than that of DM-MSCs (Fig. 2c), indicative of the enhanced capacitance of PM-MSCs. It can be observed that the broad redox peaks, appearing at 2.0–2.5 V, are primarily attributed to the pseudocapacitive intercalation/deintercalation behavior of EMIM$^+$ cations along the interlayer nanochannels of MXene films.[50] Significantly, PM-MSCs delivered a volumetric capacitance of 96 F cm^{-3}, which is 1.5 times higher than that of DM-MSCs (63 F cm^{-3}) at 50 mV s^{-1}. It can be noted that the capacitance contribution of the thin EG layer to the total capacitance of PM-MSCs is negligible, about 1.2% (Fig. S7†). Furthermore, the electrochemical impedance spectrum (EIS) of PM-MSCs displayed a higher knee frequency of 0.82 Hz and larger slope in the low frequency range (Fig. 2e), in comparison with that of DM-MSCs (0.38 Hz), reflecting enhanced capacitive behaviors and fast ion dynamics of PM-MSCs. These results further demonstrate that the pre-intercalation of the ionic liquid electrolyte into MXene films with expanded interlayer spacing can intensively accommodate more available ions, provide a high ion-accessible surface area and low ion transport resistance, and thus dramatically increase the capacitance of electrochemically active MXene materials.[41,47] In addition, it

should be mentioned that the water content in the ionic liquid electrolyte was about 0.6 wt%, which didn't exert an effect on the stability of ionic liquids tested at 3 V (Fig. S8†).[51] And this result was also demonstrated from the polarization curves of PM-MSCs (Fig. S9†).

To maximize the electrochemical performance of planar PM-MSCs (Fig. 3a), we further optimized the film thickness of MXene microelectrodes. It can be seen that, when increasing the film thickness from 2 to 3.2 μm for PM-MSCs tested at 0.3 mA cm^{-3}, the volumetric capacitance gradually increased from 98 to 122 F cm^{-3} (Fig. 3b and S10†). The discharge times of PM-MSCs based on the 3.2 and 3.6 μm-thick films almost remained unchanged, which is likely ascribed to the inadequately pre-embedded electrolyte ions for thicker microelectrodes. Furthermore, we also investigated the effect of the type of pre-intercalated and tested ionic liquid on the performance of PM-MSCs, using the 3.2 μm-thick MXene films. Specifically, the four ionic liquids are EMIMBF$_4$, 1-ethyl-3-methylimidazolium bis(trifluoromethylsulfonyl)imide (EMIMTFSI), N$_{11,1O1,1O2}$BF$_4$ (see chemical structure in Fig. S11†) and 1-butyl-3-methylimidazolium hexafluorophosphate (BMIMPF$_6$), which were correspondingly denoted as PM-MSCs-EB, PM-MSCs-ET, PM-MSCs-NB and PM-MSCs-BP, respectively. Both the CV curves obtained at 50 mV s^{-1} (Fig. 3d) and the galvanostatic charge and discharge (GCD) profiles measured at 0.4 mA cm^{-2}
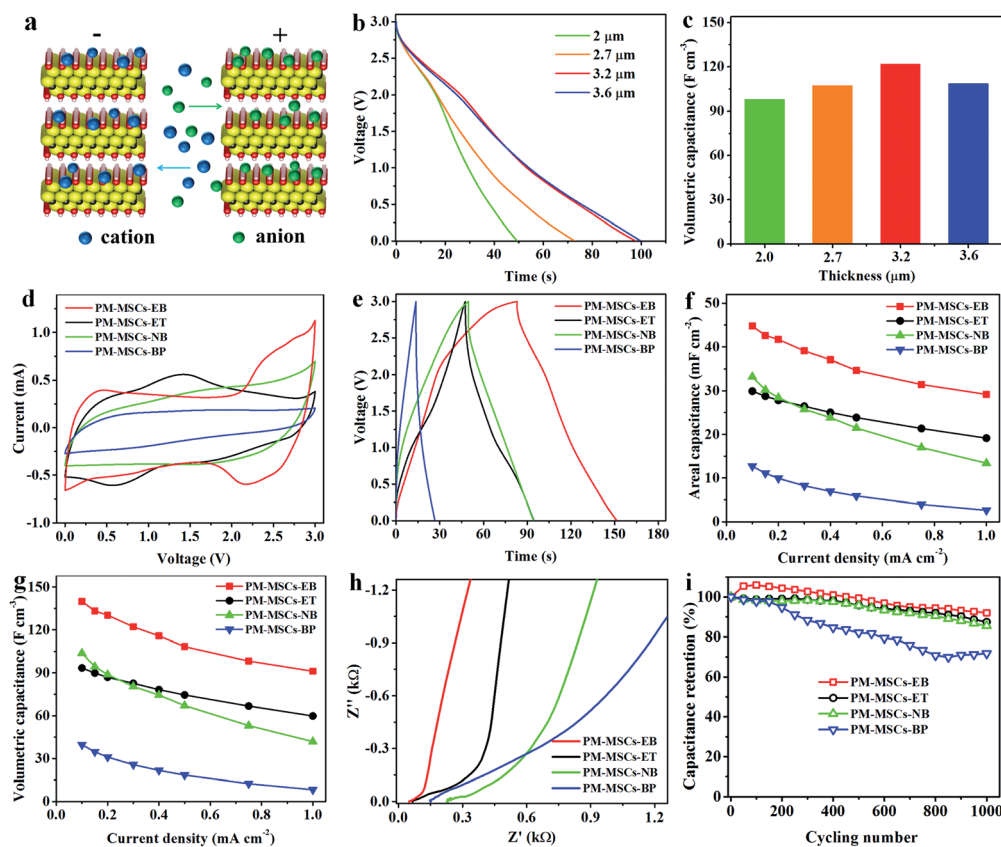

Fig. 3 Electrochemical performance of PM-MSCs measured in different ionic liquids. (a) Schematic diagram of parallel ion transfer between MXene nanosheet based films. (b) Discharge profiles and (c) volumetric capacitance of PM-MSCs-EB with various electrode thicknesses, tested at 0.3 mA cm^{-3}. (d) CV curves obtained at 50 mV s^{-1}, (e) GCD profiles measured at 0.4 mA cm^{-2}, (f) areal capacitance, (g) volumetric capacitance, (h) EIS spectra and (i) cycling stability of PM-MSCs-EB, PM-MSCs-ET, PM-MSCs-NB and PM-MSCs-BP, respectively.

This journal is © The Royal Society of Chemistry 2019

J. Mater. Chem. A, 2019, 7, 9478–9485 | 9481

(Fig. 3e) revealed that all the PM-MSCs working in these ionic liquids can be well operated at 3 V, exceeding those of aqueous-electrolyte based M-MSCs, for instance, 0.6 V in 1 M H_2SO_4,[34] 0.8 V in polyvinyl alcohol (PVA)/H_3PO_4,[23] and 1.0 V in 3 M H_2SO_4.[52] In comparison with PM-MSCs-ET, PM-MSCs-NB and PM-MSCs-BP, PM-MSCs-EB showed a larger integration area of the CV curve and longer discharge time in the GCD profile, indicative of the higher capacitance of PM-MSCs-EB. It should be pointed out that the redox peaks of PM-MSCs-EB and PM-MSCs-ET resulted from the insertion and extraction of $EMIM^+$ cations during charge and discharge.[46,53] As a result, PM-MSCs-EB tested at a low current density of 0.1 mA cm^{-2} delivered a high areal capacitance of 44 mF cm^{-2} (Fig. 3f) and volumetric capacitance of 139 F cm^{-3} (Fig. 3g), both of which are much higher than those of PM-MSCs-ET (29 mF cm^{-2} and 93 F cm^{-3}), PM-MSCs-NB (33 mF cm^{-2} and 103 F cm^{-3}) and PM-MSCs-BP (12 mF cm^{-2} and 39 F cm^{-3}). Moreover, PM-MSCs-EB, tested at a high current density of 1.0 mA cm^{-2}, also presented excellent rate capability, with a considerable areal capacitance of 29 mF cm^{-2} and volumetric capacitance of 91 F cm^{-3}, out-performing PM-MSCs-ET (19 mF cm^{-2} and 60 F cm^{-3}), PM-

MSCs-NB (13 mF cm^{-2} and 42 F cm^{-3}) and PM-MSCs-BP (3 mF cm^{-2} and 8 F cm^{-3}). This can be well explained by the lower equivalent series resistance (ESR) of PM-MSCs-EB (50 Ω) (Fig. 3h and S12†) and higher ionic conductivity of $EMIMBF_4$ (14 mS cm^{-1}, Fig. S13†),[54] as compared with those of PM-MSCs-ET (67 Ω and 8.4 mS cm^{-1}),[55] PM-MSCs-NB (233 Ω and 2.2 mS cm^{-1})[56] and PM-MSCs-BP (152 Ω and 1.5 mS cm^{-1}).[57] Also, based on the frequency at the maximum imaginary specific capacitance (C''), PM-MSCs-EB showed a high characteristic frequency of 0.15 Hz (Fig. S14†), demonstrative of the fast ion transfer of $EMIMBF_4$ between MXene nanosheets. In addition, PM-MSCs-EB exhibited outstanding cycling stability at 1.5 mA cm^{-2}, with a capacitance retention of 92% after 1000 cycles, much better than those of previously reported $Ti_3C_2T_x$ film supercapacitors in EMIMTFSI (80%, 1000 cycles).[45,46]

To meet the booming demand for wearable, flexible and integrated microelectronics, we further constructed all-solid-state PM-MSCs based on a microelectrode thickness of 3.2 μm and the $EMIMBF_4$/PVDF-HFP ionogel electrolyte (denoted as PM-MSCs-EBIE, Fig. 4a), with an exceptional ionic conductivity of 25 mS cm^{-1} (Fig. S15†).[19] From Fig. 4b and c, it can be seen
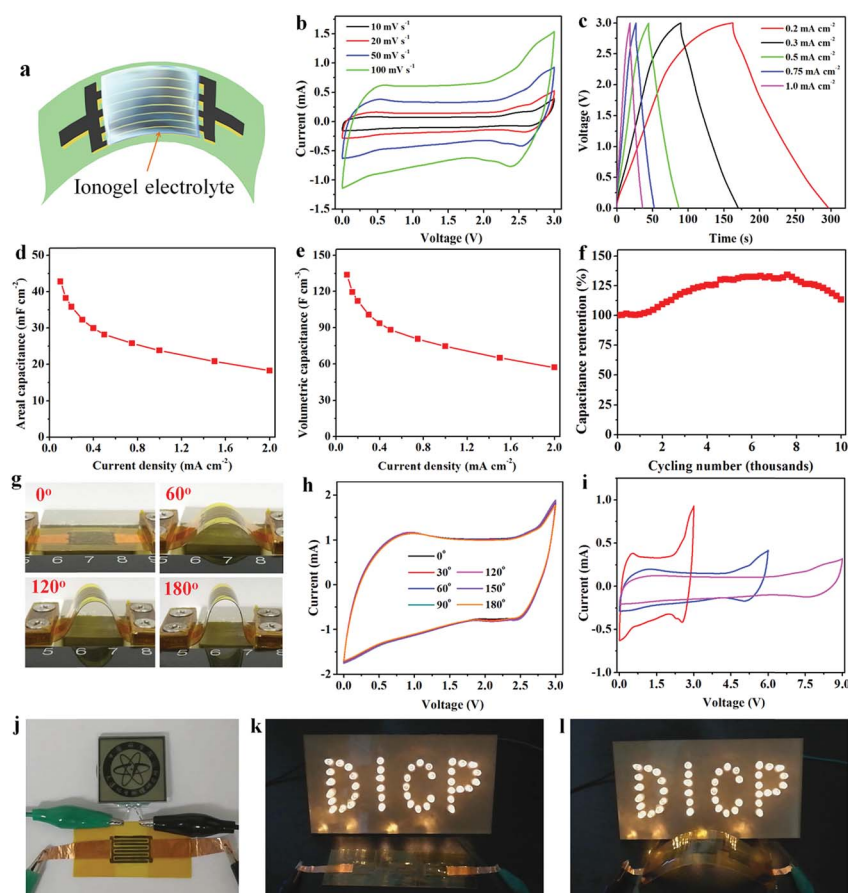

Fig. 4 Electrochemical performance of the all-solid-state PM-MSCs-EBIE. (a) Schematic of PM-MSCs-EBIE using the ionogel electrolyte. (b) CV curves tested from 10 to 100 mV s^{-1}. (c) GCD profiles measured from 0.2 to 1 mA cm^{-2}. (d) Areal capacitance and (e) volumetric capacitance obtained from 0.1 to 2 mA cm^{-2}. (f) Cyclability tested at 1.0 mA cm^{-2}. (g) Optical images of flexible PM-MSCs-EBIE at various bending angles. (h) CV curves measured at different bending states at 200 mV s^{-1}. (i) CV curves of serially connected PM-MSCs-EBIE from 1 to 3 cells, tested at 50 mV s^{-1}. (j) Optical image of the DICP logo display powered by one PM-MSCs-EBIE. (k and l) Optical images of "DICP" letters composed of 42 LED lights, powered by three serially connected PM-MSCs-EBIE in flat (k) and bending (l) states.

9482 | *J. Mater. Chem. A*, 2019, **7**, 9478–9485

This journal is © The Royal Society of Chemistry 2019

that both CV curves and GCD profiles of PM-MSCs-EBIE are largely similar to those of PM-MSCs-EB, suggestive of coherent electrochemical behavior. Notably, PM-MSCs-EBIE at a low current density of 0.1 mA cm^{-2} delivered areal (Fig. 4d) and volumetric (Fig. 4e) capacitances of 42 mF cm^{-2} and 133 F cm^{-3}, respectively, both of which were slightly lower than those of PM-MSCs-EB (44 mF cm^{-2} and 139 F cm^{-3}, Fig. 3f and g). At a high current density of 1 mA cm^{-2}, PM-MSCs-EBIE still offered an impressive areal capacitance of 24 mF cm^{-2} and volumetric capacitance of 74 F cm^{-3}, implying exceptional rate capability. Also, PM-MSCs-EBIE displayed a lower ESR of 45 Ω compared to PM-MSCs-EB (50 Ω) because of the enhanced ionic conductivity of the ionogel electrolyte (Fig. S16†). Additionally, PM-MSCs-EBIE showed exceptional cyclability without capacitance degradation after 10 000 cycles at 1.0 mA cm^{-2} (Fig. 4f). The initial increase of capacitance is mainly attributed to the gradual increase in the ion accessible area of MXene films originating from the slow infiltration of the ionogel electrolyte. With cycling, more and more ions were gradually inserted into the inner of MXene microelectrodes, leading to the gradual increase of capacitance. It is highlighted that such a long-life cyclability of MXene based supercapacitors in ionic liquid has never been achieved. To verify the flexibility of the as-fabricated microdevices, we further examined the CV curves of PM-MSCs-EBIE in different bending states (Fig. 4g). In Fig. 4h, it is revealed that the almost overlapping CV curves tested at 200 mV s^{-1} from flat to 180° evidenced the outstanding flexibility of PM-MSCs-EBIE. Furthermore, PM-MSCs-EBIE can easily realize self-integration to effectively boost the output voltage and capacitance through continuous one-by-one transfer without the requirement of metal-based interconnections (Fig. 1k and l). For instance, the operating voltage for obtaining CV curves exhibited a monotonous increase from 3 V for one cell, 6 V for two-serially connected cells, and 9 V for three-serially connected cells (Fig. 4i). More importantly, one PM-MSCs-EBIE can easily power a DICP logo display for more than 5 min after charging for 150 s at 0.2 mA cm^{-2} (Fig. 4j). Furthermore, the three serially-connected PM-MSCs-EBIE pack can readily light the four letters of DICP composed of 42 light-emitting diodes (LEDs) in both flat (Fig. 4k) and bending (Fig. 4l) states, indicating the dramatic potential of the PM-MSCs-EBIE as a stand-alone micropower source for microelectronics.

Ragone plots are shown in Fig. 5a and b to compare the areal and volumetric energy densities and power densities of PM-MSCs in different ionic liquids with those of other previously reported M-MSCs and commercially available energy storage microdevices. Notably, PM-MSCs-EB and PM-MSCs-EBIE offered high areal energy densities of 13.9 and 13.3 μW h cm^{-2}, respectively, much higher than those of PM-MSCs-ET (9.3 μW h cm^{-2}), PM-MSCs-NB (10.4 μW h cm^{-2}), PM-MSCs-BP (4.0 μW h cm^{-2}), PM-MSCs tested in 1 M H$_2$SO$_4$ (PM-MSCs-SA, 1.5 μW h cm^{-2}, Fig. S17†) and PM-MSCs tested in PVA/H$_2$SO$_4$ (PM-MSCs-PSA, 4.1 μW h cm^{-2}, Fig. S18†), and superior to those of the reported M-MSCs (Table S1†), such as MXene//Co–Al-layered double hydroxide (Co–Al-LDH) asymmetric MSCs (10.8 μW h cm^{-2}),[43] clay-like MXene MSCs (0.76 μW h cm^{-2})[21] and MXene-reduced graphene oxide (rGO) MSCs (2.2 μW h cm^{-2}).[44]
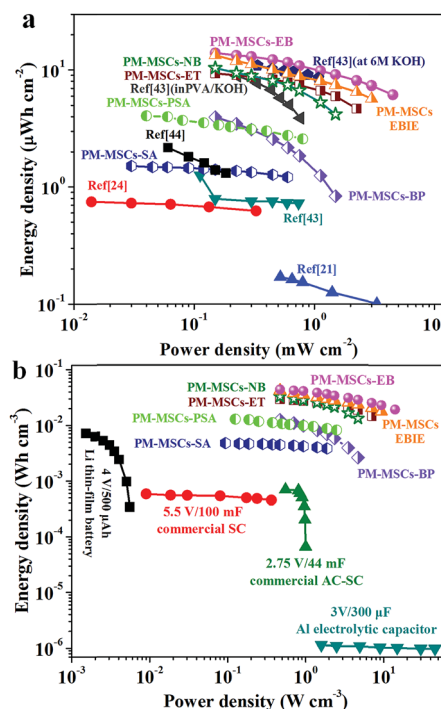

Fig. 5 Ragone plot to compare (a) areal and (b) volumetric energy density and power density of PM-MSCs in different electrolytes with other reported M-MSCs (MXene//Co–Al-LDH,[43] Ti$_3$C$_2$T$_X$ hybrid ink,[43] Ti$_3$C$_2$T$_X$ ink,[24] Ti$_3$C$_2$T$_X$/graphene aerogel,[44] and HF-etched Ti$_3$C$_2$T$_X$ [21]) and commercially available energy storage devices.

Moreover, PM-MSCs-EB also exhibited a high areal power density of 4.5 mW cm^{-2}.

Remarkably, PM-MSCs-EB and PM-MSCs-EBIE delivered ultrahigh volumetric energy densities of 43.7 and 41.8 mW h cm^{-3}, respectively. And both of these values are higher than those of PM-MSCs-ET (29.2 mW h cm^{-3}), PM-MSCs-NB (32.4 mW h cm^{-3}), PM-MSCs-BP (12.4 mW h cm^{-3}), PM-MSCs-SA (4.7 mW h cm^{-3}), and PM-MSCs-PSA (12.7 mW h cm^{-3}), four times higher than those of lithium thin film batteries (<10 mW h cm^{-3}), at least one order of magnitude higher than those of commercial supercapacitors (5.5 V/100 mF and 2.75 V/44 mF), and four orders of magnitude higher than that of an Al electrolytic capacitor.[17] It is noteworthy that these values of 43.7 and 41.8 mW h cm^{-3} are also 2–7 times higher than those reported for M-MSCs (Table S2†), e.g. all MXene based MSCs (18 mW h cm^{-3}),[22] MXene/rGO asymmetric MSCs (8.6 mW h cm^{-3})[58] and MXene based MSCs (6.1 mW h cm^{-3}).[59] And importantly, the value (43.7 mW h cm^{-3}) is the highest value of the reported M-MSCs to date. Furthermore, at a high power density of 14 W cm^{-3}, PM-MSCs-EB could still exhibit a considerable energy density of 19.2 mW h cm^{-3}.

Conclusions

In summary, we have demonstrated the successful construction of high-energy ionogel-based flexible and integrated MSCs using interdigital planar microelectrodes of ionic liquid pre-

This journal is © The Royal Society of Chemistry 2019

J. Mater. Chem. A, 2019, 7, 9478–9485 | 9483

intercalated MXene films, free of a metal current collector. The as-fabricated PM-MSCs with a $EMIMBF_4$/PVDF-HFP ionogel electrolyte delivered landmark areal and volumetric energy density. Moreover, all-solid-state PM-MSCs exhibited long-term stable cyclability up to 10 000 cycles without capacitance fading, exceptional mechanical flexibility, facile self-integration of bipolar cells and modularization for enhancing output voltage and capacitance. These findings validate that the pre-intercalation of ionic liquid into 2D MXene compact films, with expanded interlayer spacing, can substantially provide extended nanospacing for enhanced accommodation of electrolyte ions and establishment of a continuous ion transport network, resulting in dramatic performance enhancement of MSCs. Considering a large family of MXenes and high volumetric capacitance (currently 100–200 F cm^{-3} in ionic liquids), this work will open up a new avenue for creating ionic liquid pre-intercalated MXene films toward high-energy and flexible MSCs.

Conflicts of interest

There are no conflicts to declare.

Acknowledgements

Notes and references

1 N. A. Kyeremateng, T. Brousse and D. Pech, *Nat. Nanotechnol.*, 2017, **12**, 7–15.

2 Y. G. Wang, Y. F. Song and Y. Y. Xia, *Chem. Soc. Rev.*, 2016, **45**, 5925–5950.

3 K.-H. Choi, J. Yoo, C. K. Lee and S.-Y. Lee, *Energy Environ. Sci.*, 2016, **9**, 2812–2821.

4 S. Zheng, J. Ma, Z.-S. Wu, F. Zhou, Y. He, F. Kang, H.-M. Cheng and X. Bao, *Energy Environ. Sci.*, 2018, **11**, 2001–2009.

5 Z. T. Zhang, X. L. Chen, P. N. Chen, G. Z. Guan, L. B. Qiu, H. J. Lin, Z. B. Yang, W. Y. Bai, Y. F. Luo and H. S. Peng, *Adv. Mater.*, 2014, **26**, 466–470.

6 A. Sumboja, J. Liu, W. G. Zheng, Y. Zong, H. Zhang and Z. Liu, *Chem. Soc. Rev.*, 2018, **47**, 5919–5945.

7 Z.-S. Wu, X. Feng and H.-M. Cheng, *Natl. Sci. Rev.*, 2014, **1**, 277–292.

8 M. Beidaghi and Y. Gogotsi, *Energy Environ. Sci.*, 2014, **7**, 867–884.

9 D. Qi, Y. Liu, Z. Liu, L. Zhang and X. Chen, *Adv. Mater.*, 2017, **29**, 1602802.

10 J. Chmiola, C. Largeot, P. L. Taberna, P. Simon and Y. Gogotsi, *Science*, 2010, **328**, 480–483.

11 Z. S. Wu, K. Parvez, X. L. Feng and K. Müllen, *Nat. Commun.*, 2013, **4**, 2487.

12 Z.-S. Wu, Y.-Z. Tan, S. Zheng, S. Wang, K. Parvez, J. Qin, X. Shi, C. Sun, X. Bao, X. Feng and K. Müllen, *J. Am. Chem. Soc.*, 2017, **139**, 4506–4512.

13 J. Cai, C. Lv and A. Watanabe, *Nano Energy*, 2016, **30**, 790–800.

14 P. Huang, C. Lethien, S. Pinaud, K. Brousse, R. Laloo, V. Turq, M. Respaud, A. Demortière, B. Daffos, P. L. Taberna, B. Chaudret, Y. Gogotsi and P. Simon, *Science*, 2016, **351**, 691–695.

15 D. Pech, M. Brunet, H. Durou, P. H. Huang, V. Mochalin, Y. Gogotsi, P. L. Taberna and P. Simon, *Nat. Nanotechnol.*, 2010, **5**, 651–654.

16 J. Lin, C. Zhang, Z. Yan, Y. Zhu, Z. Peng, R. H. Hauge, D. Natelson and J. M. Tour, *Nano Lett.*, 2013, **13**, 72–78.

17 M. F. El-Kady and R. B. Kaner, *Nat. Commun.*, 2013, **4**, 1475.

18 M. M. Wu, Y. R. Li, B. W. Yao, J. Chen, C. Li and G. Q. Shi, *J. Mater. Chem. A*, 2016, **4**, 16213–16218.

19 F. Zhou, H. Huang, C. Xiao, S. Zheng, X. Shi, J. Qin, Q. Fu, X. Bao, X. Feng, K. Müllen and Z.-S. Wu, *J. Am. Chem. Soc.*, 2018, **140**, 8198–8205.

20 X. Shi, S. Zheng, Z.-S. Wu and X. Bao, *J. Energy Chem.*, 2018, **27**, 25–42.

21 N. Kurra, B. Ahmed, Y. Gogotsi and H. N. Alshareef, *Adv. Energy Mater.*, 2016, **6**, 1601372.

22 Y.-Y. Peng, B. Akuzum, N. Kurra, M.-Q. Zhao, M. Alhabeb, B. Anasori, E. C. Kumbur, H. N. Alshareef, M.-D. Ger and Y. Gogotsi, *Energy Environ. Sci.*, 2016, **9**, 2847–2854.

23 H. Li, Y. Hou, F. Wang, M. R. Lohe, X. Zhuang, L. Niu and X. Feng, *Adv. Energy Mater.*, 2017, 7, 1601847.

24 C. Zhang, M. P. Kremer, A. Seral-Ascaso, S.-H. Park, N. McEvoy, B. Anasori, Y. Gogotsi and V. Nicolosi, *Adv. Funct. Mater.*, 2018, **28**, 1705506.

25 Z. S. Wu, K. Parvez, S. Li, S. Yang, Z. Y. Liu, S. H. Liu, X. L. Feng and K. Muellen, *Adv. Mater.*, 2015, **27**, 4054–4061.

26 Z.-S. Wu, Y. Zheng, S. Zheng, S. Wang, C. Sun, K. Parvez, T. Ikeda, X. Bao, K. Müllen and X. Feng, *Adv. Mater.*, 2017, **29**, 1602960.

27 E. Eustache, C. Douard, R. Retoux, C. Lethien and T. Brousse, *Adv. Energy Mater.*, 2015, **5**, 1500680.

28 Z. Li, M. Shao, L. Zhou, R. Zhang, C. Zhang, J. Han, M. Wei, D. G. Evans and X. Duan, *Nano Energy*, 2016, **20**, 294–304.

29 J. J. Yoo, K. Balakrishnan, J. Huang, V. Meunier, B. G. Sumpter, A. Srivastava, M. Conway, A. L. Mohana Reddy, J. Yu, R. Vajtai and P. M. Ajayan, *Nano Lett.*, 2011, **11**, 1423–1427.

30 P. Zhang, F. Wang, M. Yu, X. Zhuang and X. Feng, *Chem. Soc. Rev.*, 2018, **47**, 7426–7451.

31 Y. Dong, S. Zheng, J. Qin, X. Zhao, H. Shi, X. Wang, J. Chen and Z.-S. Wu, *ACS Nano*, 2018, **12**, 2381–2388.

32 N. K. Chaudhari, H. Jin, B. Kim, D. S. Baek, S. H. Joo and K. Lee, *J. Mater. Chem. A*, 2017, **5**, 24564–24579.

33 Q. Yang, T. P. Jiao, M. Li, Y. B. Li, L. T. Ma, F. N. Mo, G. J. Liang, D. H. Wang, Z. F. Wang, Z. H. Ruan, W. J. Zhang, Q. Huang and C. Y. Zhi, *J. Mater. Chem. A*, 2018, **6**, 18525–18532.

34 M. R. Lukatskaya, O. Mashtalir, C. E. Ren, Y. Dall'Agnese, P. Rozier, P. L. Taberna, M. Naguib, P. Simon, M. W. Barsoum and Y. Gogotsi, *Science*, 2013, **341**, 1502–1505.

35 X. Zhang, Z. H. Zhang and Z. Zhou, *J. Energy Chem.*, 2018, **27**, 73–85.

36 M. Lu, H. J. Li, W. J. Han, J. N. Chen, W. Shi, J. H. Wang, X. M. Meng, J. G. Qi, H. B. Li, B. S. Zhang, W. Zhang and W. T. Zheng, *J. Energy Chem.*, 2019, **31**, 148–153.

37 A. VahidMohammadi, J. Moncada, H. Z. Chen, E. Kayali, J. Orangi, C. A. Carrero and M. Beidaghi, *J. Mater. Chem. A*, 2018, **6**, 22123–22133.

38 F. Wu, Y. Jiang, Z. Q. Ye, Y. X. Huang, Z. H. Wang, S. J. Li, Y. Mei, M. Xie, L. Li and R. J. Chen, *J. Mater. Chem. A*, 2019, **7**, 1315–1322.

39 Y. Xia, T. S. Mathis, M.-Q. Zhao, B. Anasori, A. Dang, Z. Zhou, H. Cho, Y. Gogotsi and S. Yang, *Nature*, 2018, **557**, 409–412.

40 A. D. Dillon, M. J. Ghidiu, A. L. Krick, J. Griggs, S. J. May, Y. Gogotsi, M. W. Barsoum and A. T. Fafarman, *Adv. Funct. Mater.*, 2016, **26**, 4162–4168.

41 M. R. Lukatskaya, S. Kota, Z. Lin, M.-Q. Zhao, N. Shpigel, M. D. Levi, J. Halim, P.-L. Taberna, M. W. Barsoum, P. Simon and Y. Gogotsi, *Nat. Energy*, 2017, **6**, 17105.

42 C. Zhang, B. Anasori, A. Seral-Ascaso, S.-H. Park, N. McEvoy, A. Shmeliov, G. S. Duesberg, J. N. Coleman, Y. Gogotsi and V. Nicolosi, *Adv. Mater.*, 2017, **29**, 1702678.

43 S. Xu, Y. Dall'Agnese, G. Wei, C. Zhang, Y. Gogotsi and W. Han, *Nano Energy*, 2018, **50**, 479–488.

44 Y. Yue, N. Liu, Y. Ma, S. Wang, W. Liu, C. Luo, H. Zhang, F. Cheng, J. Rao, X. Hu, J. Su and Y. Gao, *ACS Nano*, 2018, **12**, 4224–4232.

45 Z. Lin, D. Barbara, P.-L. Taberna, K. L. Van Aken, B. Anasori, Y. Gogotsi and P. Simon, *J. Power Sources*, 2016, **326**, 575–579.

46 Z. Lin, P. Rozier, B. Duployer, P.-L. Taberna, B. Anasori, Y. Gogotsi and P. Simon, *Electrochem. Commun.*, 2016, **72**, 50–53.

47 X. Yang, C. Cheng, Y. Wang, L. Qiu and D. Li, *Science*, 2013, **341**, 534–537.

48 A. Lipatov, M. Alhabeb, M. R. Lukatskaya, A. Boson, Y. Gogotsi and A. Sinitskii, *Adv. Electron. Mater.*, 2016, **2**, 1600255.

49 F. Shahzad, M. Alhabeb, C. B. Hatter, B. Anasori, S. Man Hong, C. M. Koo and Y. Gogotsi, *Science*, 2016, **353**, 1137–1140.

50 N. Jackel, B. Kruner, K. L. Van Aken, M. Alhabeb, B. Anasor, F. Kaasik, Y. Gogotsi and V. Presser, *ACS Appl. Mater. Interfaces*, 2016, **8**, 32089–32093.

51 Y. Zhang, R. Ye, D. Henkensmeier, R. Hempelmann and R. Chen, *Electrochim. Acta*, 2018, **263**, 47–52.

52 J. Yan, C. E. Ren, K. Maleski, C. B. Hatter, B. Anasori, P. Urbankowski, A. Sarycheva and Y. Gogotsi, *Adv. Funct. Mater.*, 2017, **27**, 1701264.

53 Y. Dall'Agnese, P. Rozier, P.-L. Taberna, Y. Gogotsi and P. Simon, *J. Power Sources*, 2016, **306**, 510–515.

54 J. Fuller, R. T. Carlin and R. A. Osteryoung, *J. Electrochem. Soc.*, 1997, **144**, 3881–3886.

55 A. B. McEwen, H. L. Ngo, K. LeCompte and J. L. Goldman, *J. Electrochem. Soc.*, 1999, **146**, 1687–1695.

56 Z. Chen, S. Liu, Z. Li, Q. Zhang and Y. Deng, *New J. Chem.*, 2011, **35**, 1596–1606.

57 J. A. Widegren, E. M. Saurer, K. N. Marsh and J. W. Magee, *J. Chem. Thermodyn.*, 2005, **37**, 569–575.

58 C. Couly, M. Alhabeb, K. L. V. Aken, N. Kurra, L. Gomes, A. M. Navarro-Suárez, B. Anasori, H. N. Alshareef and Y. Gogotsi, *Adv. Electron. Mater.*, 2018, **4**, 1700339.

59 H. B. Hu and T. Hua, *J. Mater. Chem. A*, 2017, **5**, 19639–19648.

This journal is © The Royal Society of Chemistry 2019

J. Mater. Chem. A, 2019, **7**, 9478–9485 | **9485**